Chinese Journal of
POLYMER SCIENCE

RESEARCH ARTICLE

https://doi.org/10.1007/s10118-026-3851-y
Chinese J. Polym. Sci.

Heteroatom-rich Porous Carbon for High-loading Asymmetric Single-atom Catalyst toward Efficient Zinc-air Batteries

Jia-Ming Li[a,†], Xuan-Hua Chen[a,†], Tan Yi[a], Xiao-Yu Qiao[a], Jun-Long Huang[b*], and Shao-Hong Liu[a*]

[a] *Key Laboratory for Polymeric Composite and Functional Materials of Ministry of Education, School of Chemistry, Sun Yat-sen University, Guangzhou 510006, China*
[b] *Advanced Institute for Materials Research (WPI-AIMR), Tohoku University, Sendai 980-8577, Japan*

Electronic Supplementary Information

Abstract Single-atom catalysts (SACs) are promising low-cost materials for zinc-air batteries, yet simultaneously achieving high density and high intrinsic activity of atomic sites remains a significant challenge. Herein, a sulfur and nitrogen co-doped porous carbon (SNC) featuring high heteroatom contents (16.0 wt% sulfur and 10.1 wt% nitrogen) and a hierarchical porous architecture, is developed as a robust substrate for cobalt single-atom catalysts. Benefiting from these abundant anchoring sites and synergistic S/N coordination, a high-loading Co SAC (Co/SNC, 8.9 wt%) with an asymmetric Co—S_3N_1 configuration are successfully fabricated. The unique coordination environment optimizes the electronic structure and reaction kinetics, endowing Co/SNC with outstanding oxygen reduction reaction activity ($E_{1/2}$=0.89 V), surpassing commercial Pt/C. When employed as cathode catalyst, the zinc-air battery delivers a high specific capacity (789 mAh·g_{Zn}^{-1}), peak power density (98 mW·cm^{-2}), and robust long-term durability. This work offers a promising strategy for the rational design of high-performance SACs for energy conversion devices.

Keywords Single-atom catalyst; Zinc-air battery; Asymmetric coordination; Polymer-derived carbon

Citation: Li, J. M.; Chen, X. H.; Yi, T.; Qiao, X. Y.; Huang, J. L.; Liu, S. H. Heteroatom-rich porous carbon for high-loading asymmetric single-atom catalyst toward efficient zinc-air batteries. *Chinese J. Polym. Sci.* https://doi.org/10.1007/s10118-026-3851-y

INTRODUCTION

Zinc-air batteries represent one of the most promising candidates for next-generation energy storage and conversion systems. However, their practical application is largely hindered by the sluggish kinetics of the oxygen reduction reaction (ORR) and the oxygen evolution reaction (OER) at the air cathode.[1,2] Although noble metal-based catalysts exhibit appealing electrocatalytic activity, their exorbitant cost and scarcity impede large-scale commercialization.[3–5] Therefore, the rational design and development of cost-effective, high-performance non-noble-metal electrocatalysts are urgently needed to promote the practical application of zinc-air batteries.

Single-atom catalysts (SACs), featuring well-defined electronic structures, high catalytic activity, and maximized atom utilization, have demonstrated effectiveness as low-cost catalysts for Zn-air batteries.[6,7] Their atomic precision also offers an ideal platform for elucidating structure–activity relationships at the molecular level.[8,9] Nevertheless, most reported SACs adopt a symmetric metal-nitrogen (*e.g.*, M—N_4) coordination configuration, which often leads to suboptimal electronic structures and limited intrinsic activity for the ORR. To overcome this limitation, recent efforts have demonstrated that introducing heteroatoms (denoted as A) other than nitrogen to construct asymmetric M—N_xA_y sites can break the planar symmetry of the electron density around the metal center. This asymmetry precisely modulates the electronic state and charge distribution of the active site, thereby optimizing the adsorption/desorption energies of oxygen-containing intermediates.[10,11]

To date, a variety of asymmetric heteroatom-coordinated single-atom catalysts, such as Co—N_2O_2, Co—N_3Cl_1, and Fe—N_4—S, have been developed as cathode materials for zinc-air batteries, exhibiting enhanced catalytic performance compared to their symmetric counterparts.[12–14] Nevertheless, compared to the traditional symmetric M—N_4 structure, asymmetric active sites are generally less stable under the harsh conditions of high-temperature pyrolysis, making it difficult to achieve high metal loading while maintaining the desired coordination environment.[15] On the one hand, the doping content of heteroatoms such as N and S in conventional carbon frameworks remains limited, resulting in insufficient anchoring sites for single metal atoms. On the other hand, isolated metal atoms inherently possess a high surface free energy and tend to migrate and aggregate into metallic nanoclusters or nanoparticles during high-temperature syn-

* Corresponding authors, E-mail: huang.junlong.d5@tohoku.ac.jp (J.L.H.)
E-mail: liushh27@mail.sysu.edu.cn (S.H.L.)
† These authors contributed equally to this work.
Invited Research Article
Received July 8, 2026; Accepted August 17, 2026; Published online November 4, 2026

© Chinese Chemical Society
Institute of Chemistry, Chinese Academy of Sciences

thesis. Consequently, most asymmetric SACs reported to date exhibit low metal loadings (typically <5 wt%), which restricts their catalytic performance, particularly under high current density operation in practical energy conversion devices.[16–18] Therefore, the development of carbon substrates with abundant and stable heteroatom doping is of paramount importance for constructing high loading asymmetric SACs.

Herein, inspired by our group's previously developed sulfur-assisted pyrolysis strategy, sulfur and nitrogen co-doped porous carbon (SNC) was developed as a robust substrate for the preparation of high-loading asymmetric cobalt single-atom catalysts.[19,20] The as obtained SNC not only achieves exceptionally high heteroatom doping levels (16.0 wt% S and 10.1 wt% N) but also possesses a three dimensional hierarchical porous architecture with a large surface area. Consequently, a high-loading Co single-atom catalyst (Co/SNC) featuring an asymmetric Co—S_3N_1 coordination configuration was effectively developed. Owing to the high density of these asymmetric active sites, the Co/SNC catalyst exhibited outstanding ORR activity, achieving a half-wave potential as high as 0.89 V. When employed as a cathode catalyst in Zn-air batteries, Co/SNC delivers excellent electrochemical performance, including a specific capacity of 789 mAh·g_{Zn}^{-1}, a peak power density of 98 mW·cm^{-2}, and remarkable long-term durability. This work provides a promising strategy for the rational design of high-performance cathode catalysts for Zn-air batteries.

MATERIALS AND CHARACTERIZATIONS

Details are shown in the electronic supplementary information (ESI).

RESULTS AND DISCUSSION

Fig. 1(a) shows the synthesis process of Co/SNC. In brief, a mixture of polystyrene (PS), cyclic sulfur molecules (S_8), calcium carbonate ($CaCO_3$), and melamine was pyrolyzed at 800 °C for 3 h, followed by acidic etching to remove the $CaCO_3$ template, yielding the SNC substrate. Notably, the direct pyrolysis of PS alone does not produce carbonaceous products.[21]

However, during pyrolysis, S_8 molecules undergo ring-opening polymerization to form linear polysulfide chains with diradical termini, which effectively induce dehydrogenation and crosslinking of PS, generating a thermally stable intermediate polymer network. As shown in Fig. S1 (in ESI), the as-obtained SNC exhibited a three-dimensional porous structure derived mainly from the $CaCO_3$ template. Nitrogen adsorption-desorption measurements revealed that the SNC pos-

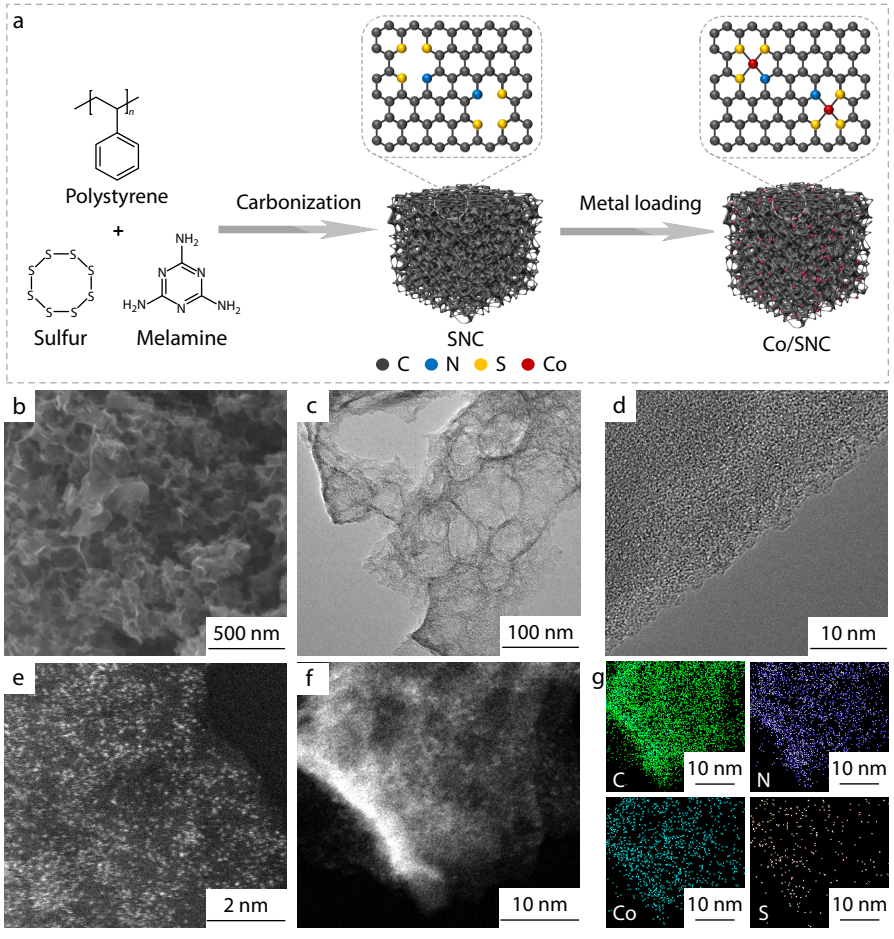


Fig. 1 (a) Schematic illustration of the synthetic process of Co/SNC; (b) SEM image, (c, d) TEM images, (e) AC HAADF-STEM image, (f) HAADF-STEM image and (g) corresponding EDS element mapping images of Co/SNC.

https://doi.org/10.1007/s10118-026-3851-y

sessed a high Brunauer-Emmett-Teller (BET) surface area of 244 $m^2 \cdot g^{-1}$ with H_4-type hysteresis loops, and the corresponding pore size distribution curve confirmed the presence of micropores and mesopores in the SNC (Fig. S2 and Table S1 in ESI).[22] Benefiting from the S_8 and melamine precursors, high contents of heteroatoms (N:10.1 wt% and S: 16.0 wt%) are detected in SNC by elemental analysis (Table S2 in ESI). The chemical composition of SNC was further investigated by X-ray photoelectron spectroscopy (XPS), which revealed the presence of C, N, and S elements (Fig. S3 in ESI).

Subsequently, Co/SNC was successfully synthesized *via* a simple two-step loading process for single cobalt atoms. Scanning electron microscopy (SEM) and transmission electron microscopy (TEM) images revealed that Co/SNC inherited the three-dimensional porous structure of SNC (Figs. 1b and 1c). Compared with SNC, Co/SNC exhibited similar nitrogen adsorption-desorption isotherms and pore size distributions, yet delivered a decreased BET surface area of 128 $m^2 \cdot g^{-1}$ (Fig. S2 and Table S1 in ESI). This phenomenon originates from the abundant incorporation of Co atoms into the pore channels, which inevitably reduces the overall BET surface area. Raman spectroscopy revealed that all samples exhibited characteristic signals at 1346 and 1590 cm^{-1}, which can be assigned to defective carbon (D-band) and graphitic carbon (G-band), respectively (Fig. S4a in ESI). Notably, Co/SNC displayed an intensified G-band intensity relative to SNC, which can be attributed to the promoted graphitization degree catalyzed by immobilized Co single atoms at 550 °C. High-resolution TEM (HRTEM) observations revealed no Co nanoclusters or nanoparticles (Fig. 1d), which is consistent with the X-ray diffraction (XRD) results (Fig. S4b in ESI). Atomic-scale bright spots can be observed in the aberration-corrected (AC) HAADF-STEM image of Co/SNC, confirming that Co exists as isolated single atoms (Fig. 1e). Additionally, HAADF-STEM and the corresponding energy-dispersive X-ray spectroscopy (EDS) element mapping (Figs. 1f and 1g) images show that C, N, Co, and S species were uniformly distributed in Co/SNC.

The chemical composition of Co/SNC was further investigated by XPS, which revealed the presence of N, S, and Co elements (Fig. S5 in ESI). The high-resolution N 1s spectrum of Co/SNC (Fig. 2a) displays peaks at 398.0, 399.7, 400.7 and 404.0 eV corresponding to pyridinic N, pyrrolic N, graphitic N, and oxidized N, respectively. In addition, the pyridinic nitrogen coordinated with a single Co atom to form Co—N bonds, as evidenced by the peak at 398.7 eV.[23] In comparison with SNC, the binding energies of pyridinic N and pyrrolic N for Co/SNC decrease by 0.25 and 0.10 eV, respectively, further proving Co—N interaction.[24] Meanwhile, the C—S—C bonds in the high-resolution S 2p spectrum shifted negatively by 0.18 eV, due to Co—S bond formation and the resulting higher electron density around sulfur (Fig. 2b).[25] The high-resolution Co 2p spectrum exhibited two main peaks at 781.0 and 796.9 eV, corresponding to the Co $2p_{3/2}$ and Co $2p_{1/2}$ spin-orbit components of $Co^{\delta+}$, respectively (Fig. 2c). No characteristic peaks corresponding to metallic Co (778.1–778.8 eV) were observed, further confirming the isolated single-atom nature of Co.[26]

A Co K-edge X-ray absorption near-edge structure (XANES) was employed to elucidate the electronic configuration and coordination environment of the Co species within the Co/SNC. The absorption edge of Co/SNC lies between those of the Co foil and CoO, indicating that the valence state of Co is between 0 and +2 (Fig. 2d). The Fourier-transformed extended X-ray absorption fine structure (EXAFS) spectrum of Co/SNC displayed two peaks at 1.34 and 1.84 Å, corresponding to Co—N and Co—S bonds, respectively (Fig. 2e).[27,28] The absence of Co—Co characteristic peaks at about 2.1 Å further confirms the atomically dispersed nature of Co sites in Co/SNC. Moreover, the Wavelet-transformed EXAFS (WT-EXAFS) spectra of Co/SNC manifested a maximum intensity at 5.9 $Å^{-1}$, consistent with Co—N/Co—S bonds, as verified by comparison with Co foil and CoPc (Fig. 2f and Fig. S6 in ESI).[29] Quantitative least-squares EXAFS fitting revealed that each Co atom in Co/SNC coordinates with three sulfur atoms and one nitrogen atom, forming an asymmetric Co—S_3N_1 structure (Fig. S7 and Table S3 in ESI). According to EA analysis, Co/SNC retained abundant heteroatoms after cobalt loading, with N and S contents of 4.0 wt% and 8.8 wt%, respectively. Benefiting from the high heteroatom content, inductively coupled plasma optical emission spectrometry (ICP-OES) measurements delivered a high Co content of 8.9 wt% for Co/SNC. To the best of our knowledge, this loading compares favorably with those of recently reported Co single-atom catalysts (Fig. 2g).

To validate the structural advantages of SNC for high-loading asymmetric SACs, sulfur-doped porous carbon (SC) and nitrogen-doped porous carbon (NC) were also synthesized as supports and subsequently loaded with cobalt, affording Co/SC and Co/NC, respectively (Figs. S8 and S9 in ESI). The sulfur and nitrogen contents are determined to be 12.2 wt% and 8.8 wt% for SC and NC, respectively, comparable to those of SNC (Table S2 in ESI). Moreover, N_2 adsorption–desorption measurements demonstrated that both SC and NC exhibited highly porous architectures, which were retained after cobalt loading (Figs. S10, S11 and Table S1 in ESI). The XRD patterns of Co/SC and Co/NC showed no discernible diffraction peaks, ruling out the presence of cobalt clusters (Fig. S12 in ESI). The XPS and EXAFS results further corroborated the absence of Co—Co bonds and confirmed the existence of isolated symmetric Co—S_4 and Co—N_4 single-atom sites in Co/SC and Co/NC, respectively (Figs. S13–S17 in ESI). Notably, although NC possesses a nitrogen content similar to that of SNC, the resulting Co/NC shows a markedly lower cobalt loading of only 3.2 wt%. Conversely, SC exhibited a sulfur level comparable to that of SNC, and Co/SC achieved a cobalt loading of 8.0 wt%, approaching that of Co/SNC (Table S2 in ESI). Overall, the above results demonstrate that the presence of sulfur dopants affords a substantially high density of Co single atoms, whereas the nitrogen dopants dictate the formation of an asymmetric coordination configuration around the metal center.

To evaluate the electrocatalytic activity of Co/SNC toward ORR, linear sweep voltammograms (LSV) were recorded using a rotating disk electrode (RDE) in O_2-saturated 0.1 $mol \cdot L^{-1}$ KOH electrolyte at a scan rate of 10 $mV \cdot s^{-1}$. As shown in Figs. 3(a) and 3(b), Co/SNC delivers an onset potential (E_{onset}) of 0.97 V and a half-wave potential ($E_{1/2}$) of 0.89 V, outperforming both of the benchmark Pt/C catalyst (E_{onset}=0.94 V, $E_{1/2}$=0.84 V) and recently reported Co single-atom catalysts

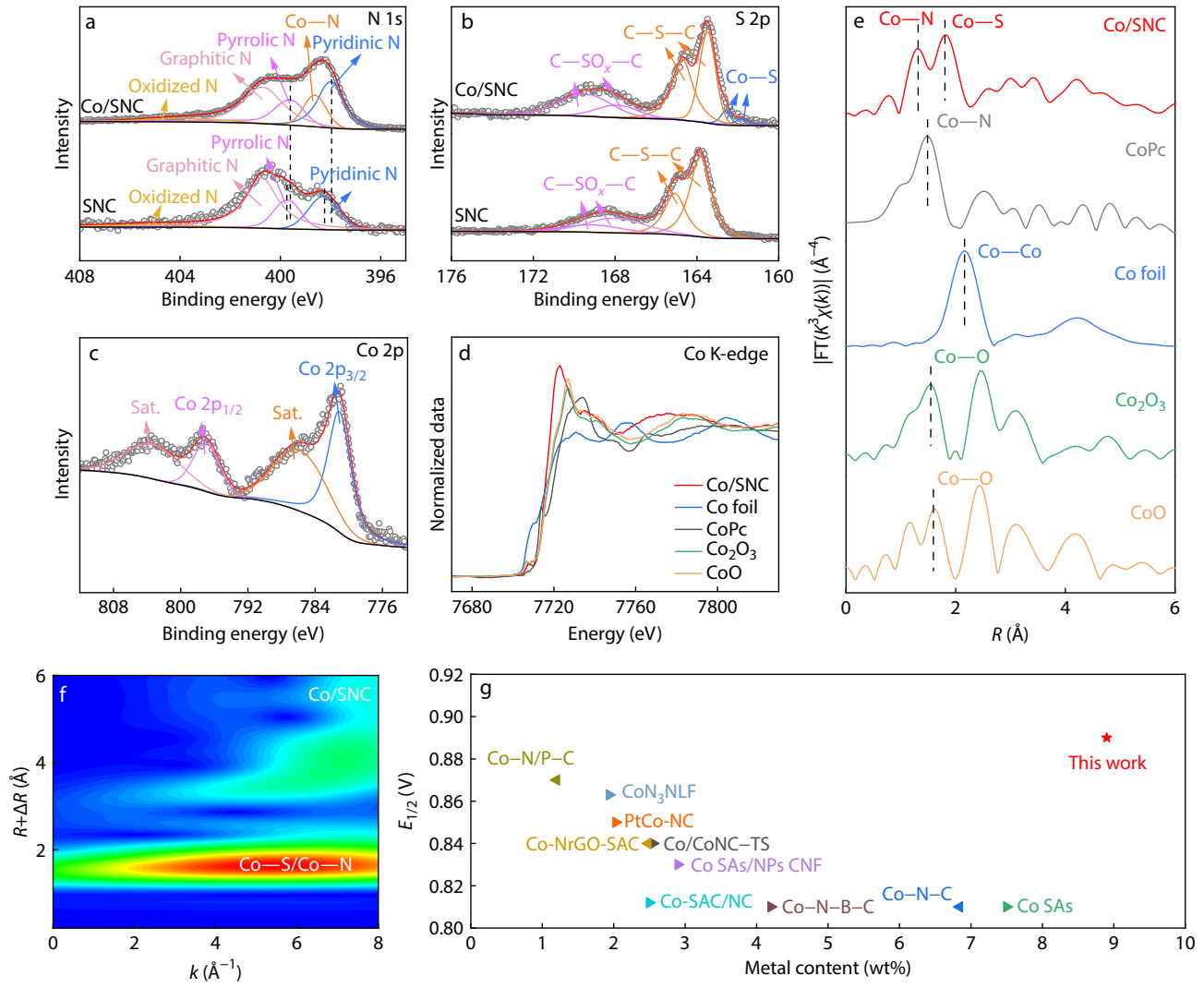


Fig. 2 High-resolution (a) N 1s and (b) S 2p XPS spectra of Co/SNC and SNC; (c) High-resolution Co 2p XPS spectra of Co/SNC; (d) Co K-edge XANES spectra; (e) Fourier transformed EXAFS spectra of Co/SNC, Co foil, CoPc, Co_2O_3, and CoO; (f) WT-EXAFS spectra of Co/SNC; (g) Single-atom loading comparison and the corresponding $E_{1/2}$ between Co/SNC and previously reported materials.

(Fig. 2g and Table S4 in ESI).[30–39] Moreover, Co/SNC demonstrated a considerably higher diffusion-limiting current density (23.8 mA·cm^{-2}) than Pt/C (4.4 mA·cm^{-2}) at 0.6 V. The well-defined current plateau observed between 0.70 and 0.20 V is characteristic of a diffusion-controlled process related to four-electron-dominated ORR pathway. To gain a deeper insight into the structural advantages of Co/SNC, the electrocatalytic performances of SNC and Co/SC were evaluated under identical conditions. As expected, owing to its lack of single-atom Co species, SNC exhibits substantially lower onset and half-wave potentials (E_{onset}=0.86 V, $E_{1/2}$=0.76 V) than Co/SNC. Notably, despite having a similar Co single atom loading, Co/SC also demonstrate considerably poorer activity, with a much lower onset and half-wave potential (E_{onset}=0.88 V, $E_{1/2}$=0.80 V) compared to Co/SNC, verifying the key role of asymmetric Co—S_3N_1 moiety in facilitating the ORR process. The superior catalytic activity of Co/SNC toward ORR is further evidenced by its smallest Tafel slope of 59.9 mV·dec^{-1}, which is considerably lower than those of SNC (69.3 mV·dec^{-1}), Co/SC (62.3 mV·dec^{-1}), and even Pt/C catalyst (91.7 mV·dec^{-1}) (Fig. 3c). Notably, SNC exhibits inferior E_{onset} and $E_{1/2}$ values compared to Pt/C, yet displays a lower Tafel slope. This result confirms that in addition to the primary contribution from the Co—S_3N_1 active sites, the hierarchical pore structure also contributes to the improved performance of Co/SNC by facilitating mass transfer.

To further elucidate the reaction kinetics of the ORR process, the LSV curves of Co/SNC were recorded at various rotation speeds. As shown in Fig. S18 (in ESI), the current densities increased with increasing rotation rate, owing to faster mass diffusion at higher speeds. The corresponding Koutecky-Levich (K-L) plots of Co/SNC exhibit good linearity and parallelism over the potential rang of 0.40–0.60 V, indicating first-order reaction kinetics with respect to the dissolved O_2 concentration (Fig. 3d). It should be noted that Co/SNC manifests a slope similar to Pt/C (Fig. S19 in ESI). Rotating ring-disk electrode (RRDE) measurements were performed to determine the hydrogen peroxide (H_2O_2) yield. As shown in Fig. 3(e), the electron transfer number of Co/SNC reaches 3.88 in the potential range of 0.20–0.80 V, corre-

sponding to a low peroxide yield of below 10%. This suggests the existence of a desirable four-electron reduction pathway from O_2 to H_2O.[40] LSV and chronoamperometric measurements further revealed that Co/SNC exhibited superior long-term stability compared to the benchmark Pt/C catalyst in O_2-saturated 0.1 mol·L^{-1} KOH (Fig. 3f). After chronoamperometric testing for 10 h, Co/SNC retained over 90% of its initial current, whereas Pt/C exhibited a rapid current decay of 80.5% under identical conditions. The results demonstrate that the heteroatom-rich carbon skeleton can effectively sta-

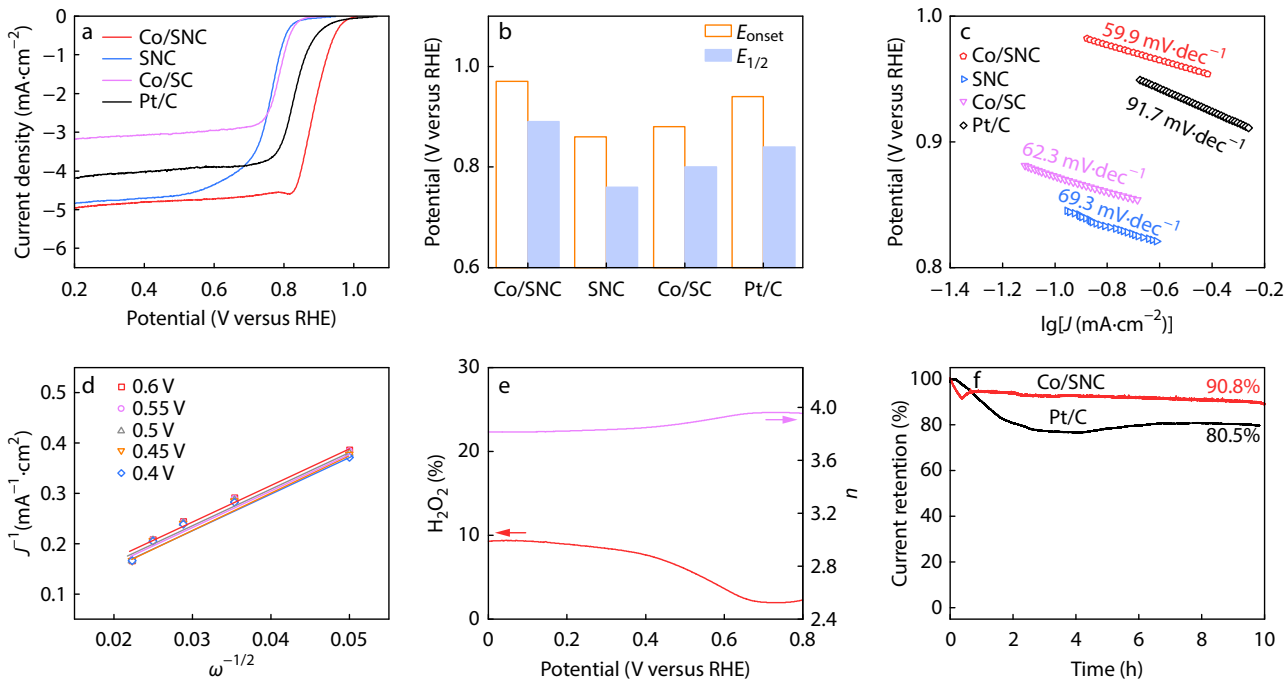


Fig. 3 (a) LSV curves, (b) the corresponding E_{onset} and $E_{1/2}$, and (c) Tafel plots of Co/SNC, SNC, Co/SC, and Pt/C; (d) K-L plots, (e) electron transfer number and H_2O_2 yield, and (f) chronoamperometric curves of Co/SNC.

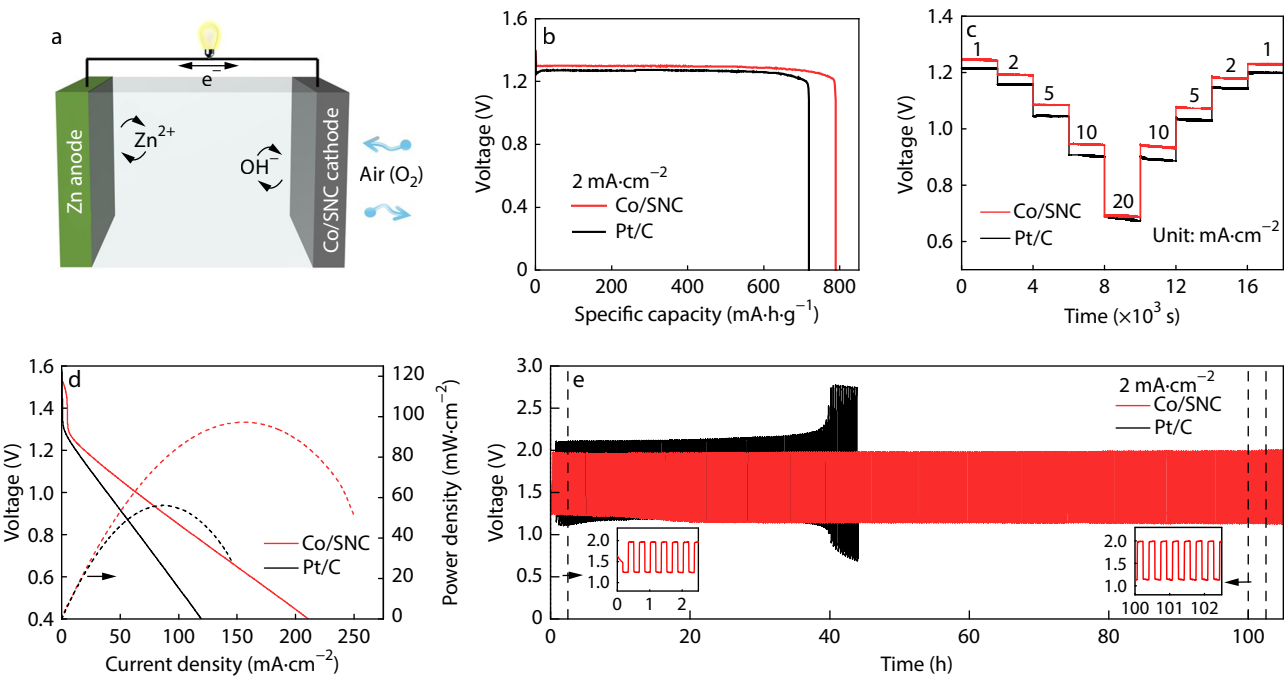


Fig. 4 (a) Schematic image of a homemade Zn-air battery; (b) Galvanostatic discharge curves at 2 mA·cm^{-2} and (c) discharge profiles at the different current densities of Zn-air batteries with Co/SNC and Pt/C; (d) Discharge curves of Zn-air batteries with Co/SNC and Pt/C catalysts and the corresponding power densities; (e) Long-term cycling tests of the rechargeable Zn-air batteries loaded with Co/SNC and Pt/C; Insets are zoomed-in profiles of typical cycles.

https://doi.org/10.1007/s10118-026-3851-y

bilize the high-loading asymmetric $Co-S_3N_1$ sites, thereby significantly enhancing catalytic durability.

To further explore the practical application of Co/SNC, a homemade Zn-air battery was assembled using Co/SNC as the cathode catalyst and zinc foil as the anode (Fig. 4a). As shown in Fig. 4(b) and Fig. S20 (in ESI), the battery with Co/SNC delivered a specific capacity of 789 mAh·g_{Zn}^{-1} and areal capacity of 18.36 mAh·cm^{-2} at 2 mA·cm^{-2} accompanied by a typical discharge plateau of 1.30 V, corresponding to 96.2% of the theoretical capacity (820 mAh·g_{Zn}^{-1}). In comparison, the battery with Pt/C catalyst achieves a specific capacity of 718 mAh·g_{Zn}^{-1} and an areal capacity of 11.33 mAh·cm^{-2} with a lower discharge plateau of 1.27 V. Moreover, the Co/SNC based battery exhibits significantly higher discharge voltages than the Pt/C based counterpart across various current densities range from 1 mA·cm^{-2} to 20 mA·cm^{-2}, confirming accelerated ORR kinetics (Fig. 4c). Notably, the battery with the Co/SNC catalyst delivered a peak power density of 98 mW·cm^{-2}, which was substantially higher than that of the Pt/C-based battery (56 mW·cm^{-2}) (Fig. 4d). As shown in Fig. S21 (in ESI), two homemade Zn-air batteries with a Co/SNC catalyst can be connected in series to power a light-emitting diode (LED) array panel. Rechargeable Zn-air batteries were further evaluated by galvanostatic charge–discharge cycling at a current density of 2 mA·cm^{-2}. Notably, the battery employing Co/SNC exhibits an initial polarization voltage hysteresis of 0.64 V and superior cycling stability, with no obvious voltage fading after over 100 h (Fig. 4e). This performance is markedly superior to that of the Pt/C based battery, whose voltage gap increases from 0.93 V in the initial cycles to 1.52 V after 45 h of cycling.

CONCLUSIONS

In summary, we successfully fabricated a sulfur-nitrogen co-doped porous carbon substrate *via* a sulfur-assisted crosslinking and templating process. The rich heteroatom functionalities of SNC serve as efficient anchoring sites, enabling the construction of a high-loading Co SAC with predominantly asymmetric $Co-S_3N_1$ coordination. This unique local structure effectively modulated the electronic density of the Co centers, endowing the resulting Co/SNC with outstanding ORR activity ($E_{1/2}$=0.89 V) and superior durability relative to Pt/C. Impressively, as an air cathode in zinc-air batteries, Co/SNC demonstrated excellent specific capacity and long-cycle durability. This work presents a viable design principle for engineering high-density asymmetric active sites, paving the way for the development of next-generation nonprecious metal catalysts for sustainable energy technologies.

Conflict of Interests

The authors declare no interest conflict.

Electronic Supplementary Information

Electronic supplementary information (ESI) is available free of charge in the online version of this article at http://doi.org/10.1007/s10118-026-3851-y.

Data Availability Statement

The data that support the findings of this study are available from the corresponding author upon reasonable request.

REFERENCES

1 Jiao, L.; Wan, G.; Zhang, R.; Zhou, H.; Yu, S. H.; Jiang, H. L. From metal–organic frameworks to single-atom Fe implanted N-doped porous carbons: efficient oxygen reduction in both alkaline and acidic media. *Angew. Chem. Int. Ed.* **2018**, *57*, 8525–8529.

2 Tomboc, G. M.; Kim, T.; Jung, S.; Yoon, H. J.; Lee, K. Modulating the local coordination environment of single-atom catalysts for enhanced catalytic performance in hydrogen/oxygen evolution reaction. *Small* **2022**, *18*, 2105680.

3 Zhu, Z.; Yin, H.; Wang, Y.; Chuang, C. H.; Xing, L.; Dong, M.; Lu, Y. R.; Casillas-Garcia, G.; Zheng, Y.; Chen, S.; Dou, Y.; Liu, P.; Cheng, Q.; Zhao, H. Coexisting single-atomic Fe and Ni sites on hierarchically ordered porous carbon as a highly efficient ORR electrocatalyst. *Adv. Mater.* **2020**, *32*, 2004670.

4 Beniya, A.; Higashi, S. Towards dense single-atom catalysts for future automotive applications. *Nat. Catal.* **2019**, *2*, 590–602.

5 Huang, R. B.; Wang, M. Y.; Xiong, J. F.; Zhang, H.; Tian, J. H.; Li, J. F. Anode optimization strategies for zinc–air batteries. *EScience* **2025**, *5*, 100309.

6 Qu, Q.; Mao, Y.; Ji, S.; Liao, J.; Dong, J.; Wang, L.; Wang, Q.; Liang, X.; Zhang, Z.; Yang, J.; Li, H.; Zhou, Y.; Wang, Z.; Waterhouse, G. I. N.; Wang, D.; Li, Y. Engineering the lewis acidity of Fe single-atom sites *via* atomic-level tuning of spatial coordination configuration for enhanced oxygen reduction. *J. Am. Chem. Soc.* **2025**, *147*, 6914–6924.

7 An, J. X.; Meng, Y.; Zhang, H. B.; Zhu, Y.; Yu, X.; Rong, J.; Hou, P. X.; Liu, C.; Cheng, H. M.; Li, J. C. Three-dimensional interconnected graphene network-based high-performance air electrode for rechargeable zinc–air batteries. *SusMat* **2024**, *4*, e201.

8 Li, J.; Sougrati, M. T.; Zitolo, A.; Ablett, J. M.; Oğuz, I. C.; Mineva, T.; Matanovic, I.; Atanassov, P.; Huang, Y.; Zenyuk, I.; Di Cicco, A.; Kumar, K.; Dubau, L.; Maillard, F.; Dražić, G.; Jaouen, F. Identification of durable and non-durable FeNx sites in Fe–N–C materials for proton exchange membrane fuel cells. *Nat. Catal.* **2021**, *4*, 10–19.

9 Xia, F.; Li, B.; An, B.; Zachman, M. J.; Xie, X.; Liu, Y.; Xu, S.; Saha, S.; Wu, Q.; Gao, S.; Abdul Razak, I. B.; Brown, D. E.; Ramani, V.; Wang, R.; Marks, T. J.; Shao, Y.; Cheng, Y. Cooperative atomically dispersed Fe–N_4 and Sn–N_x moieties for durable and more active oxygen electroreduction in fuel cells. *J. Am. Chem. Soc.* **2024**, *146*, 33569–33578.

10 Wang, Y. C.; Ma, X. B.; Ayeza, Wang, C. X.; Li, Y.; Yang, C. L.; Wang, Z. F.; Wang, C.; Hu, C.; Zhang, Y. T. A review of carbon-supported single-atom catalysts for electrochemical reactions. *New Carbon Mater.* **2024**, *39*, 407–438.

11 Li, M.; Zeng, F.; Li, S.; Hu, S.; Liu, Q.; Zhang, T.; Zhou, J.; Han, C. Unlocking high-performance organic cathodes: tailoring active group densities in covalent frameworks for aqueous zinc ion batteries. *Energy Mater. Devices* **2023**, *1*, 9370007.

12 Cao, F.; Zhang, X.; Jin, Z.; Zhang, J.; Tian, Z.; Kong, D.; Li, Y.; Li, Y.; Zhi, L. Electronegativity matching of asymmetrically coordinated single-atom catalysts for high-performance lithium–sulfur batteries. *Adv. Energy Mater.* **2024**, *14*, 2303893.

13 Zhao, C.; Chu, B.; Nian, H.; Shao, B.; Lu, Y.; Zhang, F.; Wang, Y.; Xu,

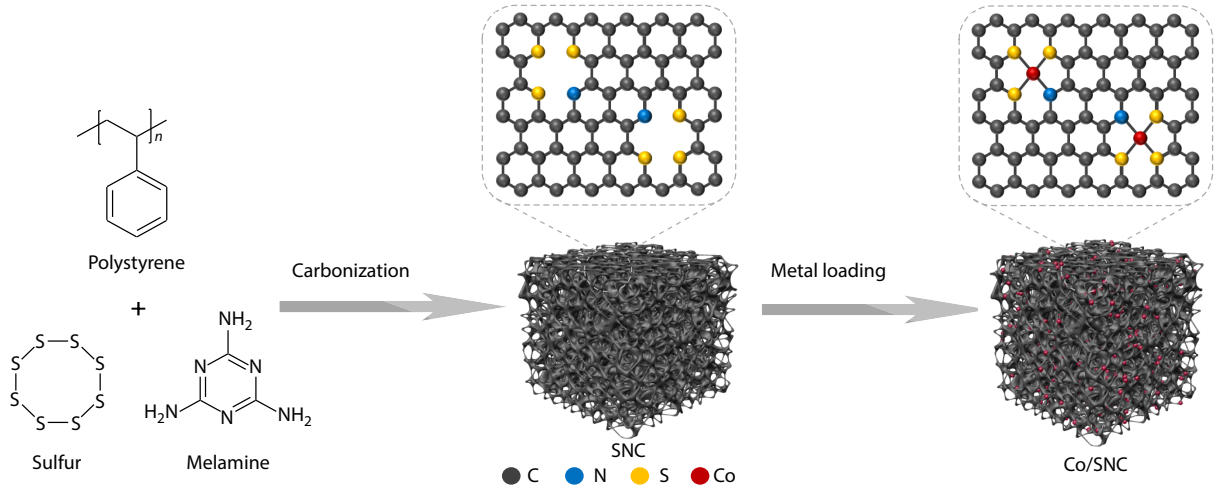
Graphical Abstract

Heteroatom-rich Porous Carbon for High-loading Asymmetric Single-atom Catalyst toward Efficient Zinc-air Batteries

Jia-Ming Li, Xuan-Hua Chen, Tan Yi, Xiao-Yu Qiao, Jun-Long Huang, and Shao-Hong Liu

Sun Yat-sen University, China; Tohoku University, Japan

In this study, we designed and synthesized heteroatom-rich S- and N-co-doped carbon (SNC). The Co/SNC catalyst (Co/SNC) derived from the SNC substrate featured high-density Co—S_3N_1 active sites. Owing to this structural advantage, Co/SNC exhibited outstanding oxygen reduction reaction (ORR) catalytic activity and excellent zinc-air battery performance.



Chinese J. Polym. Sci. 2026 *https://doi.org/10.1007/s10118-026-3851-y*

Q. Sulfur-mediated microenvironment modulation of high-density Fe-N_4 sites for high-efficiency oxygen reduction and cryotolerant quasi-solid-state zinc-air batteries. *Adv. Mater.* **2025**, *37*, e10621.

14 Xu, Y.; Zhao, Z. H.; Wang, Y.; Ma, X.; Liu, H.; Hu, J. S.; Wang, H.; Wang, D. Boosting CO_2 photoreduction *via* ligand-engineered single-atom cobalt sites in covalent organic frameworks. *Angew. Chem. Int. Ed.* **2026**, *65*, e17289.

15 Liu, L.; Chen, B.; Wu, T.; Li, M.; Chen, H.; Ge, Y.; Li, Z. Coordination reconstruction enhanced synergistic nonradical oxidation pathways in cobalt single-atom catalysts for sustained pollutant destruction. *Angew. Chem. Int. Ed.* **2025**, *64*, e202508330.

16 Wang, W. M.; Yang, Z. W.; Wu, D. X.; Wang, W. L.; Wu, Q. Y. Remote modulation of single-atom catalyst boosts high-valent cobalt-oxo species generation for water purification and detoxification. *Adv. Sci.* **2026**, *13*, e12498.

17 Sangabathula, O.; Kale, R.; Seo, J. H.; Park, C. J. Synergistic catalysis of cobalt single atoms and nanoparticles enabling stable and high-performance sodium–sulfur batteries. *Chem. Eng. J.* **2026**, *527*, 171431.

18 Cui, Z.; Wang, H.; Li, C.; Peng, W.; Liu, J. Iodine dopants facilitate tandem catalysis *via* transformation adsorption behavior for efficient electrochemical nitrate reduction reaction. *ACS Nano* **2025**, *19*, 31050−31064.

19 Tang, Y.; Cen, Z.; Ma, Q.; Zheng, B.; Cai, Z.; Liu, S.; Wu, D. A versatile sulfur-assisted pyrolysis strategy for high-atom-economy upcycling of waste plastics into high-value carbon materials. *Adv. Sci.* **2023**, *10*, 2206924.

20 Chen, X.; Yi, T.; Cen, Z.; Qiao, X.; Ji, Y.; Fu, R.; Huang, J.; Liu, S. Organosulfur-rich porous carbon cathode enables soluble-polysulfide-free and high-rate potassium-sulfur batteries. *Angew. Chem. Int. Ed.* **2026**, *65*, e05751.

21 Chung, W. J.; Griebel, J. J.; Kim, E. T.; Yoon, H.; Simmonds, A. G.; Ji, H. J.; Dirlam, P. T.; Glass, R. S.; Wie, J. J.; Nguyen, N. A.; Guralnick, B. W.; Park, J.; Somogyi, Á.; Theato, P.; MacKay, M. E.; Sung, Y. E.; Char, K.; Pyun, J. The use of elemental sulfur as an alternative feedstock for polymeric materials. *Nat. Chem.* **2013**, *5*, 518−524.

22 Jeong, U.; Kim, H.; Ramesh, S.; Dogan, N. A.; Wongwilawan, S.; Kang, S.; Park, J.; Cho, E. S.; Yavuz, C. T. Rapid access to ordered mesoporous carbons for chemical hydrogen storage. *Angew. Chem. Int. Ed.* **2021**, *60*, 22478−22486.

23 Wang, M.; Yang, W.; Li, X.; Xu, Y.; Zheng, L.; Su, C.; Liu, B. Atomically dispersed Fe–heteroatom (N, S) bridge sites anchored on carbon nanosheets for promoting oxygen reduction reaction. *ACS Energy Lett.* **2021**, *6*, 379−386.

24 Xu, S.; Feng, S.; Yu, Y.; Xue, D.; Liu, M.; Wang, C.; Zhao, K.; Xu, B.; Zhang, J. N. Dual-site segmentally synergistic catalysis mechanism: boosting CoFeSx nanocluster for sustainable water oxidation. *Nat. Commun.* **2024**, *15*, 1720.

25 Cheng, Y.; Ma, J.; Li, C.; Li, Y.; Li, H.; Zhang, C.; Yu, J.; Cai, S.; Wu, F.;

Zhu, J.; Bi, X.; Ren, Y.; Xie, Y.; Xue, Q.; He, R.; Li, Z.; Pinto-Huguet, I.; Arbiol, J.; Lu, J.; Guo, Z.; Zhang, H.; Cabot, A. Sulfur-bridged dual Fe–N_4 sites to boost lithium–sulfur battery performance. *J. Am. Chem. Soc.* **2025**, *147*, 39805–39817.

26 Zitolo, A.; Ranjbar-Sahraie, N.; Mineva, T.; Li, J.; Jia, Q.; Stamatin, S.; Harrington, G. F.; Lyth, S. M.; Krtil, P.; Mukerjee, S.; Fonda, E.; Jaouen, F. Identification of catalytic sites in cobalt-nitrogen-carbon materials for the oxygen reduction reaction. *Nat. Commun.* **2017**, *8*, 957.

27 Yang, L.; Shi, L.; Wang, D.; Lv, Y.; Cao, D. Single-atom cobalt electrocatalysts for foldable solid-state Zn-air battery. *Nano Energy* **2018**, *50*, 691–698.

28 Wang, J.; Zhao, S.; Ma, C.; Meng, H.; Zhao, C.; Zhang, X.; Nie, Y.; Lu, H.; Zong, K.; Zhang, X.; Yang, L.; Wang, X.; Chen, Z. Spin-state modulation of single-atom catalysts and coupled strong sieving effect enable efficient self-cleaning active sites in lithium-sulfur batteries. *Nano Energy* **2025**, *145*, 111406.

29 Pei, J.; Shang, H.; Mao, J.; Chen, Z.; Sui, R.; Zhang, X.; Zhou, D.; Wang, Y.; Zhang, F.; Zhu, W.; Wang, T.; Chen, W.; Zhuang, Z. A replacement strategy for regulating local environment of single-atom Co-SxN_{4-x} catalysts to facilitate CO_2 electroreduction. *Nat. Commun.* **2024**, *15*, 416.

30 Zhang, J.; Zhang, Y.; Wang, C.; Zhang, L.; Guo, Y.; Qiao, Q.; Bai, Y.; Zheng, S.; Zhang, L.; Hu, X.; Tan, M.; Tian, J. Spin-state engineering in Co–N–C catalysts enables efficient bifunctional oxygen electrocatalysis. *ACS Catal.* **2026**, *16*, 13103–13117.

31 Sun, Y.; Xiong, K.; Zhang, G.; Cheng, K.; Feng, S.; Chen, H.; Li, M.; Chen, K.; Chen, Y.; Jin, H.; Wang, S. Metalloporphyrin MOF-derived "quasi-carbon" materials featuring well-defined Co N4 sites as bifunctional electrocatalysts for enhanced zinc-air batteries performance. *Chem. Eng. J.* **2025**, *519*, 165652.

32 Liu, X.; Wang, Z.; Wang, J.; Tang, T.; Li, C.; Yu, J.; Zhang, S.; Deng, C. Unsaturated cobalt-nitrogen atomic sites in necklace-like hairy fibers towards highly efficient oxygen electrocatalysis for flexible Zn-Air battery. *Energy Storage Mater.* **2024**, *65*, 103184.

33 Zou, J.; Bao, L.; Sun, Q.; Bao, C.; Chen, H.; Liu, H. Oxygen reduction reaction catalysts for zinc-air batteries featuring single cobalt atoms in a nitrogen-doped 3D-interconnected porous graphene framework. *Small* **2025**, *21*, 2409506.

34 Cheng, Y.; Song, H.; Yu, J.; Chang, J.; Waterhouse, G. I. N.; Tang, Z.; Yang, B.; Lu, S. Carbon dots-derived carbon nanoflowers decorated with cobalt single atoms and nanoparticles as efficient electrocatalysts for oxygen reduction. *Chin. J. Catal.* **2022**, *43*, 2443–2452.

35 Qi, Y.; Liang, Q.; Song, K.; Zhou, X.; Liu, M.; Li, W.; Liu, F.; Jiang, Z.; Zou, X.; Chen, Z.; Zhang, W.; Zheng, W. Optimizing high-coordination shell of Co-based single-atom catalysts for efficient ORR and zinc-air batteries. *J. Energy Chem.* **2024**, *95*, 306–314.

36 Rao, P.; Wu, D.; Wang, T. J.; Li, J.; Deng, P.; Chen, Q.; Shen, Y.; Chen, Y.; Tian, X. Single atomic cobalt electrocatalyst for efficient oxygen reduction reaction. *EScience* **2022**, *2*, 399–404.

37 Cheng, Y.; Gong, X.; Tao, S.; Hu, L.; Zhu, W.; Wang, M.; Shi, J.; Liao, F.; Geng, H.; Shao, M. Mechano-thermal milling synthesis of atomically dispersed platinum with spin polarization induced by cobalt atoms towards enhanced oxygen reduction reaction. *Nano Energy* **2022**, *98*, 107341.

38 Xu, C.; Wu, J.; Chen, L.; Gong, Y.; Mao, B.; Zhang, J.; Deng, J.; Mao, M.; Shi, Y.; Hou, Z.; Cao, M.; Li, H.; Zhou, H.; Huang, Z.; Kuang, Y. Boric acid-assisted pyrolysis for high-loading single-atom catalysts to boost oxygen reduction reaction in Zn-air batteries. *Energy Environ. Mater.* **2024**, *7*, e12569.

39 Sun, M.; Jiang, Y.; Song, H.; Zhang, J.; Yin, G.; Cui, Y.; Zhang, C.; Yin, G.; Lu, S. Efficient ORR facilitated by Co single atoms bridged with nitrides. *Adv. Funct. Mater.* **2025**, *35*, 2504982.

40 Chen, Y.; Huang, J.; Chen, Z.; Shi, C.; Yang, H.; Tang, Y.; Cen, Z.; Liu, S.; Fu, R.; Wu, D. Molecular engineering toward high-crystallinity yet high-surface-area porous carbon nanosheets for enhanced electrocatalytic oxygen reduction. *Adv. Sci.* **2022**, *9*, e2103477.

https://doi.org/10.1007/s10118-026-3851-y